Analytical modeling of synthetic fiber ropes subjected to axial loads. Part I: A new continuum model for multilayered fibrous structures

Seyed Reza Ghoreishi, Patrice Cartraud, Peter Davies, Tanguy Messager

Analytical modeling of synthetic fiber ropes subjected to axial loads. Part I: A new continuum model for multilayered fibrous structures

Seyed Reza Ghoreishi [a], Patrice Cartraud [a], Peter Davies [b], Tanguy Messager [c]

[a] *Institut de recherche en Génie civil et Mécanique (GéM), Ecole Centrale de Nantes, 1, Rue de la Noe, BP92101, 44321 Nantes Cedes 03, France*

[b] *IFREMER, Materials and Structures group BP70, 29280 Plouzané, France*

[c] *Université de Nantes, Nantes Atlantique Universités, Institut de recherche en Génie civil et Mécanique (GéM), Ecole Centrale de Nantes, BP92101, 44321 Nantes, France*

Synthetic fiber ropes are characterized by a very complex architecture and a hierarchical structure. Considering the fiber rope architecture, to pass from fiber to rope structure behavior, two scale transition models are necessary, used in sequence: one is devoted to an assembly of a large number of twisted components (multilayered), whereas the second is suitable for a structure with a central straight core and six helical wires ($1 + 6$). The part I of this paper first describes the development of a model for the static behavior of a fibrous structure with a large number of twisted components. Tests were then performed on two different structures subjected to axial loads. Using the model presented here the axial stiffness of the structures has been predicted and good agreement with measured values is obtained. A companion paper presents the second model to predict the mechanical behavior of a $1 + 6$ fibrous structure.

Keywords: Fiber rope; Yarn; Aramid; Multilayered structures; Analytical model; Testing

1. Introduction

Synthetic fiber rope mooring systems, which are often composed of steel chain at the ends and a central synthetic fiber rope, are increasingly finding applications as offshore oil exploration goes to deeper sites. Previous researchers have shown that such mooring lines provide numerous advantages over steel mooring lines

(steel wire ropes and chains), particularly in deep water applications for which the large self-weight of steel lines is prohibitive (Beltran and Williamson, 2004; Foster, 2002). It is therefore essential to be able to model the mechanical behavior of very long synthetic mooring lines in order to reduce the need for expensive tests under varying parameters and operating conditions.

Large synthetic fiber ropes are assemblies of millions of fibers and characterized by a very complex architecture and a hierarchical structure in which the base components (fiber or yarn) are modified by twisting operations. This structure is then a base component for the next higher structure. Its hierarchical structure leads to the hierarchical approach where the top is the fiber rope and the bottom is the base components, with several different types of elements between the base component and the fiber rope, i.e. yarn, assembled yarn and strand. Fig. 1 illustrates this hierarchical structure.

Considering the fiber rope architecture, it consists of two different types of structure: one is a structure with a central straight core and six helical components (1 + 6), whereas the second is an assembly of a large number of twisted components (multilayered), see Fig. 2. So to pass from fiber to rope structure, two scale transition models are necessary, used in sequence. The results of the model at each level can be used as input data for the model at the next higher level. Use of this approach from the lowest level, at which mechanical properties are given as input, to the highest level of the rope determines the rope properties. Based on this strategy, the transition models can be used to analyze synthetic fiber ropes of complex cross-section. Fig. 3 shows the typical hierarchy ranking from the smallest level to the highest level for a 205 ton break load fiber rope.

The focus of this paper is the modeling of the static behavior of a fibrous structure with a large number of twisted components subjected to axial loads, starting from the mechanical behavior of the base component, and the geometric description of the rope structure.

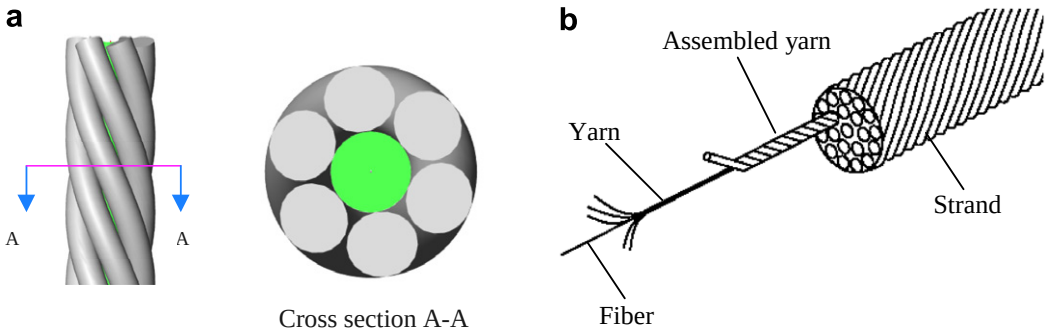

Fig. 1. Synthetic fiber rope structure. (a) Fiber robe with 1 + 6 strands and (b) construction of a strand.

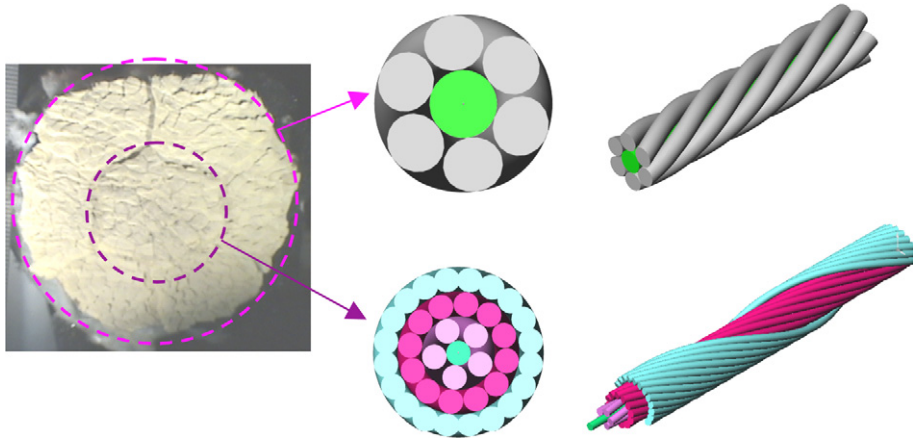

Fig. 2. Cross-section of a synthetic fiber rope (205 ton break load); the rope represents a 1 + 6 structure, core and strands are assemblies of a large number of twisted components.

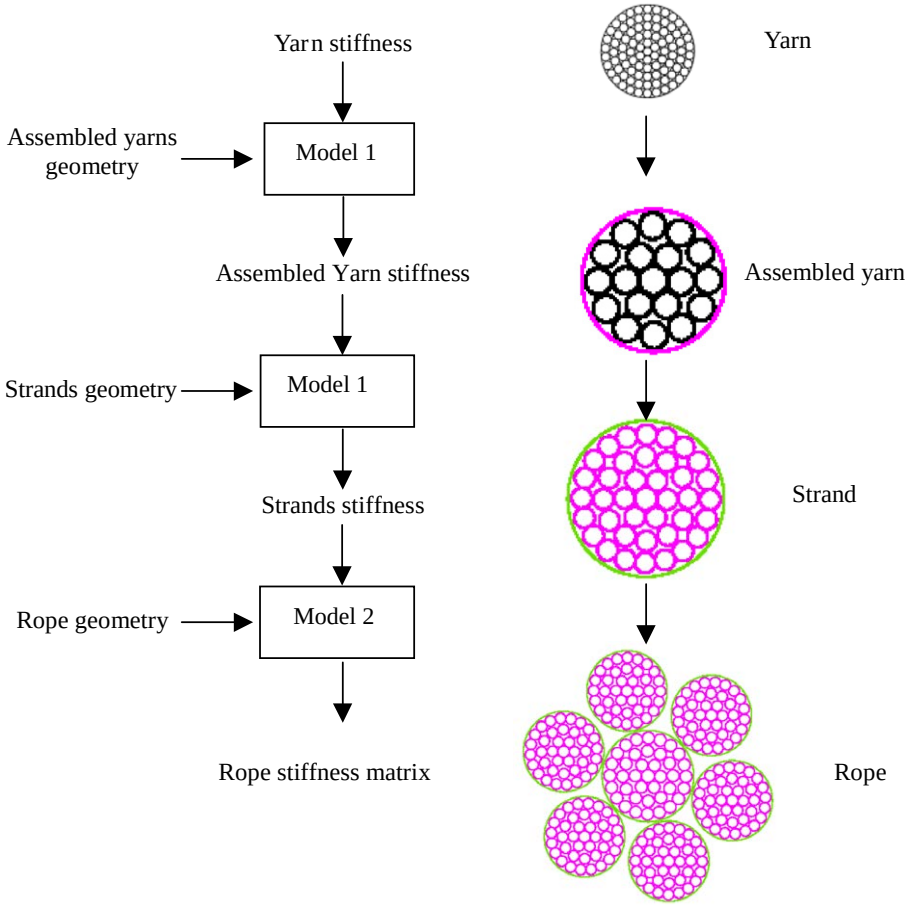

Model 1: for a structure with a large number of components.
Model 2: for a 1+6 structure.

Fig. 3. The typical hierarchy ranking from the smallest level to the highest level for a 205 ton break load fiber rope.

In Section 2, a description of the structure (geometry and behavior) is given, then, in Section 3, we present an overview of the existing mechanical models of such structures. In Section 4, a new continuum model is developed. The analytical models are compared in Section 5. Tensile tests have been performed, to provide the experimental data that are described in Section 6. In Section 7, we demonstrate the accuracy of the models by comparing their predictions to experimental results.

2. Structure description

Let us consider a multilayered structure in which each component follows a regular helical path round a central axis of the structure. The geometry of each component is characterized by the pitch length, P (length of one turn of the twist, or reciprocal of twists per unit length) and the lay angle, α, measured with respect to the structure Z axis. The component's centerline is then an helical curve of radius r.

The pitch length P, is the same at all radial positions, but the lay angle will increase from zero at the center to a maximum at the external surface of the structure, α_e, as shown in Fig. 4.

It may be noted that the component cross-sections are elliptical in the plane perpendicular to the Z axis. Therefore, the lay angle of a component at a radial position r_i, denoted by α_i can be calculated using the following expression:

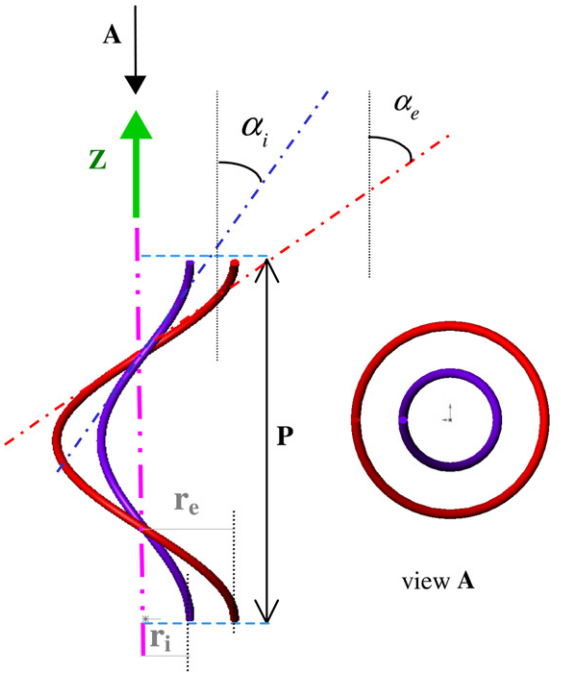

Fig. 4. An arbitrary component at a radial position r_i and a component at the outer surface of the structure with a radial position r_e.

$$\tan \alpha_i = \frac{2\pi r_i}{P} \tag{1}$$

For marine applications, the fiber ropes are subjected to axial loads, and the axial behavior of such structures exhibits coupling between tension and torsion due to the helical design of the components. Thus, the overall behavior can be expressed in the form:

$$\begin{Bmatrix} F_z \\ M_z \end{Bmatrix} = \begin{bmatrix} k_{\varepsilon\varepsilon} & k_{\varepsilon\theta} \\ k_{\theta\varepsilon} & k_{\theta\theta} \end{bmatrix} \begin{Bmatrix} u_{z,z} \\ \theta_{z,z} \end{Bmatrix} \tag{2}$$

where $u_{z,z}$ denotes the overall axial strain, $\theta_{z,z}$ the twist angle per unit length, F_z the axial force and M_z the torque. The four stiffness matrix components $k_{\varepsilon\varepsilon}$, $k_{\theta\theta}$, $k_{\theta\varepsilon}$ and $k_{\varepsilon\theta}$ are pure tensile, pure torsion and coupling terms respectively. Moreover, the stiffness matrix should be symmetric, as can be shown from Betti's reciprocal theorem.

3. Earlier models

This work is concentrated on structures with a large number of components (constitutive elements). As noted by Raoof and Hobbs (1988), since the structure consists of a large number of components, the bending moments and torque in individual components can be neglected. Several authors have developed analytical models to predict the global elastic constants providing the relationship between loads and strains for such multilayered structures, based on a knowledge of the component material and geometry of the structure.

Two categories of these models are presented: semi-continuous models developed for metallic cables and models specifically presented for synthetic cables.

3.1. Semi-continuous models

Homogenization is a well known method in solid mechanics, and can be used for the continuum modeling of a discrete system composed of a large number of identical repetitive elements. With an appropriate

choice of the material parameters, one can accurately represent the global behavior of the real system. This method was first applied to cable modeling by Hobbs and Raoof (1982). It is the orthotropic sheet model that has been described in detail by Raoof (1983) and then extended by Raoof and his associates over two decades.

In this model the classical twisted rod theories for the behavior of helical laid wires has been extended to include a set of kinematic compatibility conditions. The individual layer of wires is replaced by an equivalent cylindrical orthotropic sheet, which is assumed to be thin and to be in a plane stress state.

As in the case of composite laminates, four elastic constants are necessary. Two of them are obtained directly from the mechanical properties of the wires. The other two are related to the contact stiffness between adjacent wires in the layer. The complete structure is then treated as a discrete set of concentric orthotropic cylinders. The orthotropy axes correspond to those of a fiber composite material in which the fibers have the same lay angle as the wires in the corresponding layer.

Another semi-continuous model was developed by Blouin and Cardou (1989), and later extended by Jolicoeur and Cardou (1994, 1996). This also consists of replacing each layer with a cylinder of orthotropic, transversely isotropic material. In this model the elastic constants can be used as free, adjustable, parameters, or else estimated rationally from contact mechanics equations as in the case of the orthotropic sheet model.

Once the cable is modeled using such continuum approach, analytical solutions for elementary loadings can be derived (Crossley et al., 2003a,b).

These semi-continuous models take into account friction between constituents. However, some elastic constants are obtained from contact mechanics, considering layer components have circular cross-section. It can be seen from Fig. 2 that this is not the case for fiber ropes. Moreover, due to the homogenization process, the accuracy of this model increases when the number of wires in a given layer increases. Lastly, these models are tedious to use, and since they are non-linear, they require numerical solving.

Despite these limitations, the model of Raoof and Hobbs (1988), briefly presented in Section 3.3, will be applied here in section 5.

3.2. Synthetic fiber ropes models

In this category the simplest model is that of Hoppe (1991) in which the structure and the components are assumed to be subjected to pure tensile forces, the bending and torsional stiffness for both of them being neglected. Contact and friction between the components are also neglected, but such an approximation is justified for monotonic axial loading. It should be noted that this analytical model provides only the overall tensile behavior.

Leech et al. (1993), presented a more complex quasi-static analysis of fiber ropes and included it in a commercial software: fiber rope modeller or FRM (2003). Their analysis is based on the principle of virtual work and can take frictional effects into account. The program computes tension and torque from their dependence on elongation and twist.

Another model was developed by Rungamornrat et al. (2002), and later extended by Beltran et al. (2003) and Beltran and Williamson (2004). These models are very similar with that of Leech but they have concentrated on a damage model to take into account the degradation of rope properties as a function of loading history.

Leech's model appears to be very sophisticated, with an accurate mechanical modeling of the components of the fiber ropes behavior and their interactions. Moreover, the cross-section geometry can be described using different forms of arrangement of components (see Section 3.5). Therefore, Leech's model can be considered as a reference model, but it requires resolution.

Hereafter, the synthetic fiber ropes models of Hoppe (1991) and Leech et al. (1993) are briefly presented and then a new continuum model will be developed from the Hoppe's one to analysis the structure with a large number of twisted components.

3.3. Raoof's model

Raoof and his associates have worked extensively on the behavior of metallic structures with a large number of wires so that the bending moments and torque in individual wires become much less significant than

they are in six and seven wire cables (Hobbs and Raoof, 1982; Raoof, 1983; Raoof and Hobbs, 1988; Raoof, 1991; Raoof and Kraincanic, 1995a; Raoof and Kraincanic, 1995b). In these studies a great deal of attention has been paid to the inter-wire contact phenomena and friction has been taken fully into account. By treating each layer of wires as an orthotropic sheet with non-linear properties determined using the mechanical contact theories and assuming Coulomb friction, it has been possible to establish the stiffness matrix in the presence of an axial load.

The main features of this model are presented hereafter, in the case of metallic multilayered structure with an isotropic material.

These authors have established a set of non-linear simultaneous equations to analyse the kinematics of each layer of wires, providing a set of compatible strains in the anisotropic cylinder with a core (for more details see Raoof and Hobbs (1988)). The elastic behavior of each orthotropic sheet in the local coordinate system (t,b,n), see Fig. 5, can be expressed in the following matrix form:

$$\begin{Bmatrix} \varepsilon_{tt} \\ \varepsilon_{bb} \\ \varepsilon_{tb} \end{Bmatrix} = \begin{Bmatrix} S_{11} & S_{12} & 0 \\ S_{12} & S_{22} & 0 \\ 0 & 0 & S_{66} \end{Bmatrix} \begin{Bmatrix} \sigma_{tt} \\ \sigma_{bb} \\ \sigma_{tb} \end{Bmatrix} \tag{3}$$

where S_{ij}, ε and σ are the compliance, the strains and stresses referred to the axes of orthotropy parallel and normal to the wire axes, respectively.

The compliance parallel to the wire axis S_{11} is straightforward, reflecting the ratio between the sheet area and the wire area $(4/\pi)$:

$$S_{11} = \frac{4}{\pi E} \tag{4}$$

where E is the Young's modulus for the wire material, and the coupling term S_{12} is given by

$$S_{12} = -\nu S_{11} \tag{5}$$

where ν is Poisson's ratio.

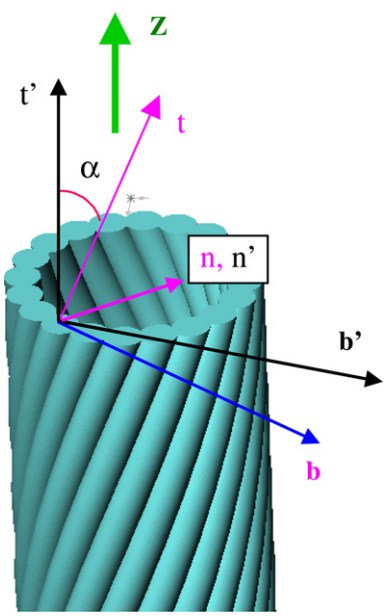

Fig. 5. Local and global coordinate systems for a layer of wires.

The compression compliance, S_{22}, has been expressed as

$$S_{22} = \frac{1}{\pi E}\left(4(1-v^2)\left[\frac{1}{3} + \ln\frac{1.25D}{\left(\frac{P_c D(1-v^2)}{E}\right)^{1/2}}\right] - 2(1-v^2)\right) \tag{6}$$

where D is the wire diameter and, P_c is the contact load per unit length on the contact area which is obtained from Hertzian contact theory for the contact of two parallel cylinders. The contact load, P_c, is determined numerically by using an iterative method.

The shear compliance, S_{66}, is determined from other results of the contact theory (Mindlin, 1949):

$$S_{66} = \frac{S_{22}}{1-v}\left(1 - \frac{\delta_l}{\delta_{l\max}}\right)^{-1/2} \tag{7}$$

where δ_l is the line contact displacement for a given total perturbation in structure axial strain, and $\delta_{l\max}$ is the corresponding displacement at the onset of full-sliding condition.

The stiffness (or compliance) has been shown to be a function of the amplitude of the load variation about the mean. For small changes of axial force the stiffness is larger than it is for bigger variations. Small changes do not overcome the inter-wire friction, while larger changes do, causing sliding and a lower effective modulus.

In this study, the stiffness matrix results of this model for two extreme cases are presented: the lower bound or full-slip, correspond to $\delta_l = \delta_{l\max}$ and the upper bound or no-slip for $\delta_l = 0$.

Once the stiffness matrix of all the layers (for a given axial preload) has been found, in order to obtain the behavior of the structure, the stiffness matrix of each layer is transformed into the global coordinate system of the structure (t', b', n'), see Fig. 5, and the summation of the stiffness of all the layers enables the global behavior of the structure to be established.

It should be noted that to apply this model to a multilayered fibrous structure, Young's modulus of the component material is obtained from axial stiffness of components in the direction of their axis, see section 4. In addition, Poisson's ratio, v, according to the volume constant deformation assumption, has been set to 0.5.

3.4. Hoppe's model

The work of Hoppe (1991) based on purely geometrical considerations, allows a model of behavior of this type of structure under a simple tensile force to be determined. This model requires the knowledge of the tensile properties of the components and the construction parameters of the structure, i.e. the number of layers, the number of components in each layer and the lay angle of each layer. This model is based on the following hypotheses: the geometry of the structure is multilayered with the helical component having circular section; at the local and global levels, the base components and the structure work only in traction in the direction of their axis (bending and torsion are neglected); the section of the structure remains plane, and perpendicular to its axis after deformation; deformation of the structure is at constant volume; strains and friction effects due to contact between components are neglected.

Using these hypotheses, the elongation of each component is determined as a function of those of the structure, and then the axial force in each component is determined. The projection of the force on the structure axis and summing for all the components enables a closed-form expression for the global behavior (only axial stiffness) of the structure to be established. In section 4, a closed-form analytical solution, for stiffness matrix components, will be developed which is based on Hoppe's model.

3.5. Leech's model

Leech et al. (1993) presented a model whose formulation is based on the principle of virtual work to analyze fiber ropes. This model is integrated in a commercial software (FRM, 2003) to predict the behavior of the synthetic cables subjected to an axial load. This model differs from Hoppe's model by the following aspects: at the global level, the behavior of the structure is characterized by coupling between tension and torsion phenomena using a 2×2 stiffness matrix; friction effects due to contact and the relative motions

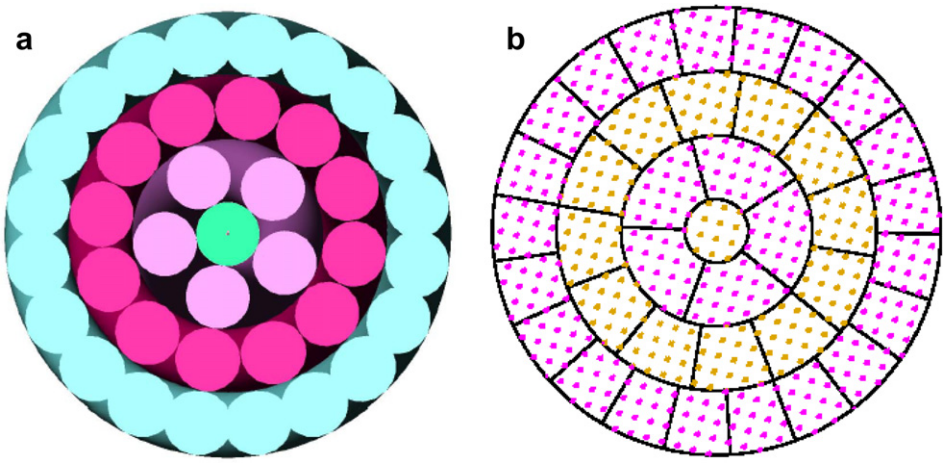

Fig. 6. Multilayered geometry of structure for various models: (a) Raoof, Hoppe and Leech (layered packing geometry) and (b) Leech (wedge geometry).

between components are considered; the geometry of the structure is multilayered, and two extreme rope geometry descriptions in transverse deformation have been considered: Layered packing geometry and Wedge geometry, see Fig. 6.

For layered packing geometry, it is assumed that a bundle of parallel identical components with circular cross-section is twisted in the assembly to form a structure with a core, surrounded by a layer of equally wound components, this layer enclosed by another layer and so on until all the components are used. Each layer is a helical structure of many components and each helix has the same pitch length but a different lay angle.

For wedge geometry, the components in the same level are allowed to deform transversely and change their shape to a wedge or truncated wedge. The equivalent helix radius is the radius of the center of area of the wedge. Within each layer the packing factor (PF) is introduced to take into account the presence of the voids in the layer that can be defined by the ratio of the area of material to the layer cross-sectional area. It can be expressed by

$$PF_i = \frac{n_i A_c / \cos \alpha_i}{2\pi r_i W_i} \tag{8}$$

where n_i, A_c and W_i are the number of components in layer i, component cross-section area and the width of the layer i respectively. It should be noted that for a given PF, the width of the layer will be defined and vice versa.

The estimation of the frictional forces that develop between the components in a structure is based on the classical slip-stick model where the friction force is assumed to develop between two contact surfaces in the direction opposite to the relative slip of these two surfaces. Six sliding modes have been presented and it was noted that, for the twisted structure under axial loading, the only significant frictional contribution (and even that is small) comes from the axial sliding mode (Leech et al., 1993; Leech, 2002).

In the present study, FRM software was used to obtain the results for Leech's model, with the wedge geometry option. First, the structure is defined. Essentially, this consists of specifying the number of components in each layer with the appropriate twist and the nature of the packing at that layer. Second, the dimensional and tensile properties of the components must be provided. Most are single parameters, but the non-linear force–strain relations can be defined in the software by the coefficients of fourth order polynomials. In this study the force–strain relations were considered linear and derived from test data.

The stiffness matrix is obtained in two steps. First, we let $\theta_{z,z} = 0$ and vary the axial strain, $u_{z,z}$, about a given value (0.01), to calculate F_z and M_z through the FRM software, which leads to $k_{\varepsilon\varepsilon}$ and $k_{\theta\varepsilon}$ from Eq. (1). In the same way, $k_{\varepsilon\theta}$ and $k_{\theta\theta}$ will be obtained by setting to 0 the axial strain, $u_{z,z}$, and varying $\theta_{z,z}$.

4. Continuum model

All the models presented above require the construction parameters of the structure such as number of layers, number of components in each layer (see Fig. 6) and lay angle of each layer (see Fig. 5). These are not always easy to define precisely for fiber rope structures, see Fig. 2, where it appears difficult to model the strand cross-section as a multilayered structure. In addition, these models are integrated in programs and numerical analysis is necessary (except for the Hoppe model which presented a closed-form expression but only for the pure tensile behavior of the structure with no torsion and coupling terms).

Here, an analytical model with a closed-form expression and model geometry more in agreement with the real geometry of the structure will be established. This involves an extension of Hoppe's model (Hoppe, 1991) which is based on the same hypotheses, as in the initial model, with an exception which is detailed in the next paragraph.

In the literature, the structures are described using a multilayered geometry, but in the present model we do not consider them like an assembly of layers, but rather as a continuum formed by a set of coaxial helixes. These helixes have the same number of turns per unit length, and their section amounts to a material point, and that describe the geometry of a constituent element. It is in this sense that this model is termed a continuum model. Moreover, within the structure the packing is assumed to be uniform. Therefore, the geometric input data for this model are restricted to the external structure radius, the pitch length and a packing factor value. In addition, the present model can describe coupling behavior between traction and torsion.

The stress–strain (force–strain) properties of the material which are introduced into the model are, in general, taken to correspond to the actual force–strain properties of the component as obtained from experiments. The relation between force–strain is assumed linear and Young's modulus of the component material is given by

$$E_c = k_c/A_c \tag{9}$$

where k_c is the component axial stiffness (slope of the force–strain curve) and A_c is the cross-section area of the component.

4.1. Axial strain of components

In the present model, the components are assumed to be subjected to pure tensile forces, the bending and torsion stiffness are neglected. In axial loading, with traction and torsion, the axial strain of each component is composed of two different parts: the first results from the elongation of the structure, whereas the second is due to its rotation. For small strains, it is possible to separate these phenomena, the axial deformation of the component is expressed therefore by

$$\varepsilon_{tt} = \varepsilon_{tt}^{A} + \varepsilon_{tt}^{R} \tag{10}$$

where t is the tangent to the component center line, ε_{tt}^{A} and ε_{tt}^{R} are the axial strains of the component due to the elongation and to the rotation of the structure respectively.

4.1.1. Elongation

Let λ_z be the extension ratio (ratio of deformed length to initial length of the structure) measured along the structure axis, and λ_r the corresponding extension ratio for a component whose initial and final radial positions are r_0 and r, respectively, see Fig. 7(a). The extension ratios, λ_z and λ_r, are defined as follows:

$$\begin{cases} \lambda_z = \frac{L}{L_0} = 1 + u_{z,z} \\ \lambda_r = \frac{l}{l_0} = 1 + \varepsilon_{tt}^{A} \end{cases} \tag{11}$$

As the volume is supposed to remain constant, the initial and final radial positions of each component can be related by the following expression:

$$\lambda_z = \left(\frac{r_0}{r}\right)^2 \tag{12}$$

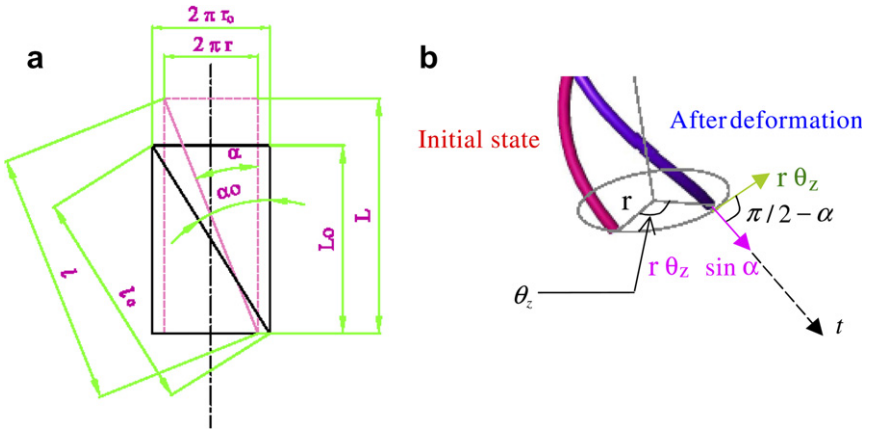

Fig. 7. Component before and after deformation; (a) elongation and (b) rotation of the structure.

If α_0 is the lay angle of this component in the initial state, one has:

$$\tan \alpha_0 = \frac{2\pi r_0}{P_0} \tag{13}$$

since after deformation the pitch length, P, determined by $P = P_0\lambda_z$, the corresponding lay angle α in the deformed state is given by

$$\tan \alpha = \frac{\tan \alpha_0}{\lambda_z^{3/2}} \tag{14}$$

Let us consider a structure having the initial length L_0, and bounded by planes perpendicular to the structure axis. The initial length of a component of lay angle α_0 is

$$l_0 = L_0/\cos \alpha_0 \tag{15}$$

the axial length in the deformed state being $\lambda_z L_0$, the corresponding component length in the deformed state is

$$l = (\lambda_z L_0)/\cos \alpha \tag{16}$$

using Eqs. (13)–(16), the component extension ratio λ_r can be expressed as follows:

$$\lambda_r^2 = \left(\lambda_z \frac{\cos \alpha_0}{\cos \alpha}\right)^2 = \lambda_z^2 \cos^2 \alpha_0 + \frac{\sin^2 \alpha_0}{\lambda_z} \tag{17}$$

which yields ε_{tt}^A from $(11)_2$.

4.1.2. Rotation

When the structure undergoes a relative rotation, θ_z, between the two end sections of length L_0, the axial strain of the component due to this rotation is expressed by

$$\varepsilon_{tt}^R = \frac{\Delta l}{l_0} \tag{18}$$

where Δl is defined by (see Fig. 7(b))

$$\Delta l = r\theta_z \sin \alpha \tag{19}$$

substituting (12), (15) and (19) into expression (18), we obtain:

$$\varepsilon_{tt}^R = \frac{r_0}{\sqrt{\lambda_z}} \theta_{z,z} \sin \alpha \cos \alpha_0 \tag{20}$$

where $\theta_{z,z}$ is the twist angle per unit length defined by

$$\theta_{z,z} = \frac{\theta_z}{L_0} \tag{21}$$

However, in general, for a given structure, its outer diameter, r_{eo}, is known, as well as the value of the lay angle on the outer layer, α_{eo}. Since for all the components the pitch length, P, is the same, the lay angle of an arbitrary component with a radial position of r_o, can be written as a function of the parameters of the outer layer:

$$\tan\alpha_o = \frac{r_o}{r_{eo}}\tan\alpha_{eo} \tag{22}$$

using Eqs. (14) and (22), one obtains:

$$\begin{cases} \cos^2\alpha = \dfrac{r_{eo}^2\lambda_z^3}{r_{eo}^2\lambda_z^3 + r_o^2\tan^2\alpha_{eo}} \\ \sin^2\alpha = \dfrac{r_0^2\tan^2\alpha_{eo}}{r_{eo}^2\lambda_z^3 + r_o^2\tan^2\alpha_{eo}} \end{cases} \tag{23}$$

While taking into account the expressions (11) and substituting relations (17) and (20) into Eq. (10), the total axial strain of the component is given by

$$\varepsilon_{tt} = \varepsilon_{tt}^A + \varepsilon_{tt}^R = \left[\sqrt{\lambda_z^2\cos^2\alpha_o + \frac{\sin^2\alpha_o}{\lambda_z}} - 1\right] + \frac{r_o}{\sqrt{\lambda_z}}\theta_{z,z}\sin\alpha\cos\alpha_o \tag{24}$$

where $\sin\alpha$ is given according to Eq. $(23)_2$, which are functions of extension ratio, λ_z, and the outer layer parameters associated to the initial geometry (r_{eo} and α_{eo}). Otherwise, $\cos\alpha_o$ and $\sin\alpha_o$ are given by substituting $\lambda_z = 1$ into the relation (23). Therefore, for an arbitrary point at a radial position r_o, the axial strain in the local coordinate system, ε_{tt}, is a function of two independent variables, λ_z and r_o.

4.2. Stiffness matrix derivation

In this model the components are assumed to be purely tensile elements with a uniaxial behavior that can be represented by

$$\sigma_{tt} = E\varepsilon_{tt} \tag{25}$$

where t is the tangent to the component centerline (see Fig. 5). In order to obtain the stiffness matrix the stress in the local coordinate system, σ_{tt}, is transformed to the global cylindrical coordinate system (r, θ, z):

$$\begin{cases} \sigma_{zz} = \sigma_{tt}\cos^2\alpha \\ \sigma_{z\theta} = \sigma_{tt}\cos\alpha\sin\alpha \end{cases} \tag{26}$$

therefore, the total axial force and torque are obtained by integration of the stresses on the cross-section area of the structure in the initial state:

$$\begin{cases} F_z = PF_g\int_0^{2\pi}\int_0^{r_{eo}}\sigma_{tt}\cos^2\alpha\; r_o\,\mathrm{d}r_o\,\mathrm{d}\theta \\ M_z = PF_g\int_0^{2\pi}\int_0^{r_{eo}}\sigma_{tt}\cos\alpha\sin\alpha r_o^2\,\mathrm{d}r_o\,\mathrm{d}\theta \end{cases} \tag{27}$$

where σ_{tt} is obtained from (24) and (25) and $\cos\alpha$ and $\sin\alpha$ from (23). The global packing factor (PF_g) is introduced to take into account the presence of the voids in the whole of the cross-sectional area of the structure. It can be expressed by

$$PF_g = \left[NA_c\frac{\int_0^{2\pi}\int_0^{r_{eo}} r_o\,\mathrm{d}r_o\,\mathrm{d}\theta}{\int_0^{2\pi}\int_0^{r_{eo}}\cos\alpha_o r_o\,\mathrm{d}r_o\,\mathrm{d}\theta}\right] \Big/ (\pi r_{eo}^2) \tag{28}$$

where N is the total number of components in the structure.

After integration of the relations (27) using the *Maple*™ software, and rewriting the results in the matrix form, Eq. (2), the stiffness matrix components, for the linear material, are expressed as follows:

$$
\begin{cases}
k_{\varepsilon\varepsilon} = 2\pi E_c r_{eo}^2 PF_g \lambda_z^{2.5} \left[\dfrac{\ln\left(\dfrac{1}{2} + \tan^2\alpha_{eo} + \dfrac{\lambda_z^3}{2} + \sqrt{(1+\tan^2\alpha_{eo})(\lambda_z^3+\tan^2\alpha_{eo})}\right)}{\tan^2\alpha_{eo}(\lambda_z - 1)} \right. \\
\qquad \left. - \dfrac{\sqrt{\lambda_z}\ln(\lambda_z^3+\tan^2\alpha_{eo}) + \ln\left(\frac{1}{2} + \frac{\lambda_z^3}{2} + \lambda_z^{1.5}\right) - \sqrt{\lambda_z}\ln(\lambda_z^3)}{\tan^2\alpha_{eo}(\lambda_z - 1)} \right] \\
k_{\varepsilon\theta} = 2\pi E_c r_{eo}^3 PF_g \lambda_z^{4.5} \left[\dfrac{\ln(\lambda_z^3+\tan^2\alpha_{eo}) + \dfrac{\lambda_z^3}{(\lambda_z^3+\tan^2\alpha_{eo})} - \ln(\lambda_z^3) - 1}{\tan^3\alpha_{eo}} \right] \\
k_{\theta\varepsilon} = \frac{2}{3}\pi E_c r_{eo}^3 PF_g \\
\qquad \times \left[\dfrac{1}{4}\lambda_z(-1-\lambda_z^3)\left(\ln\left(\dfrac{1}{2} + \tan^2\alpha_{eo} + \dfrac{\lambda_z^3}{2} + \sqrt{(1+\tan^2\alpha_{eo})(\lambda_z^3+\tan^2\alpha_{eo})}\right)\right.\right. \\
\qquad \left. + 2\sqrt{(1+\tan^2\alpha_{eo})(\lambda_z^3+\tan^2\alpha_{eo})}\right) - \dfrac{1}{2}\lambda_z^{1.5}(\tan^2\alpha_{eo} - \lambda_z^3\ln(\lambda_z^3+\tan^2\alpha_{eo})) \\
\qquad \left. \times -\dfrac{1}{4}\lambda_z(-1-\lambda_z^3)\left(\ln\left(\dfrac{1}{2} + \dfrac{\lambda_z^3}{2} + \lambda_z^{1.5}\right) + 2\lambda_z^{1.5}\right) - \dfrac{1}{2}\lambda_z^{4.5}\ln(\lambda_z^3)\right] / [\tan^3\alpha_{eo}(\lambda_z - 1)] \\
k_{\theta\theta} = \frac{2}{3}\pi E_c r_{eo}^4 PF_g \lambda_z^3 \dfrac{\left[\tan^2\alpha_{eo} - \dfrac{\lambda_z^6}{\lambda_z^3+\tan^2\alpha_{eo}} + \lambda_z^3 - 2\lambda_z^3(\ln(\lambda_z^3+\tan^2\alpha_{eo}) - \ln(\lambda_z^3))\right]}{\tan^4\alpha_{eo}}
\end{cases}
\tag{29}
$$

the stiffness matrix is a function of only the extension ratio of the structure, λ_z, global packing factor, PF_g, and the outer layer geometrical parameters of the structure in the initial state (r_{eo} and α_{eo}). Since the stiffness matrix components depend on the strain, this model is essentially non-linear, but for the interval [1.001 1.04] of extension ratio (practical strain range for aramid), λ_z, the results can be considered as constant. In the following, the results for the same axial strain ($\lambda_z = 1.01$) are presented.

5. Models comparison

The previous models have been applied to a strand of a 205 ton aramid cable of known construction parameters (given by the cable supplier) shown in Table 1.

Table 1
Available construction parameters for strand of 205 T aramid cable

Outer diameter	18.3 (mm)
Pitch length	275 (mm)
Components number	42
Component axial stiffness, k_c[a]	346.1 kN

[a] k_c obtained from experiments.

Table 2
Necessary input data for all models

Models	Input data
Raoof and Hoppe	*Pitch length*, number of layers, components number per layer, component radius, Young's modulus of component
Leech	*Pitch length*, number of layers, component number per layer, components radius, *component axial stiffness*, k_c, PF for each layer
Continuum	*Strand radius*, *Pitch length*, Young's modulus of component, PF_g

Table 2 shows the input data necessary for all models.

Comparing Tables 1 and 2 shows that input data are missing for all the models. A sensitivity analysis has been performed elsewhere by Ghoreishi (2005), and the results have shown that the overall behavior is not sensitive to these missing values for the practical structures of interest here ($\alpha_{eo} \leqslant 15°$). Some illustrative parts of this sensitivity analysis are reported hereafter.

As it has been previously mentioned, it is practically difficult to represent the strand cross-section with a multilayered structure. Therefore, several multilayered discretizations can be a priori defined. From the value of the strand radius and assembled yarn surface, it has been considered that the strand was made with four layers. The results obtained with the Leech's model corresponding to three different multilayered discretizations are given in Table 3, with very small differences.

The influence of the packing factor has also been studied, since this parameter is not defined at the local scale (i.e. in each layer) when the Leech's model is used. A four layers discretization with respectively 1, 6, 14 and 21 assembled yarns in each layer, has been considered, with three different values of the radius of the assembled yarn. For a given value of this radius, the packing factor of the layers 2–4 was constant and calibrated in order to obtain a cross-section radius consistent with the strand radius value. The results are listed in Table 4, where it can be checked that they are slightly sensitive to the packing factor values.

Therefore, for the present study, the values for the missing data were taken as follows:

Number of layers is chosen to be 4.

Component numbers for each layer are 1, 6, 14 and 21 and the PF in each layer are 1, 0.75, 0.88 and 0.89 respectively.

On the other hand, Eq. (28) gives a global packing factor, $PF_g = 0.86$. This value is in agreement with the previous values used in the Leech's model, which shows that both models have the same quantity of material in the cross-section of the structure.

Table 3
Results obtained for Leech's model for different multilayer discretizations of the strand made of 42 assembled yarns distributed in four layers

Multilayered discretization	$k_{\varepsilon\varepsilon}$ (10^3 kN)	$k_{\varepsilon\theta}$ (kN m)	$k_{\theta\varepsilon}$ (kN m)	$k_{\theta\theta}$ (N m^2)
$1+6+14+21$	14.1	13.3	13.0	21.7
$1+7+14+20$	14.1	13.1	12.8	21.4
$3+8+13+18$	14.1	13.0	12.7	21.5

Table 4
Results obtained for Leech's model for different values of Packing factor

Assembled yarn radius (mm)	PF of layers 2–4	$k_{\varepsilon\varepsilon}$ (10^3 kN)	$k_{\varepsilon\theta}$ (kN m)	$k_{\theta\varepsilon}$ (kN m)	$k_{\theta\theta}$ (N m^2)
1.31	0.866	14.1	13.3	13.0	21.7
1.35	0.921	14.1	12.9	12.7	21.1
1.38	0.958	14.1	12.9	12.7	21.0

Table 5
Results obtained for different models applied to the strand of 205 T aramid cable

Models		$k_{\varepsilon\varepsilon}$ (10^3 kN)	$k_{\varepsilon\theta}$ (kN m)	$k_{\theta\varepsilon}$ (kN m)	$k_{\theta\theta}$ (N m^2)	$\frac{k_{\varepsilon\theta}-k_{\theta\varepsilon}}{k_{\varepsilon\theta}}$ (%)
Raoof	Full slip	14.1	13.5	13.7	19.0	1.48
	No-slip	14.7	7.72	9.27	105	20
Hoppe		14.1	–	–	–	–
Leech	$\mu = 0$	14.1	13.3	13.0	21.7	2.26
	$\mu = 0.15$	14.1	13.3	13.5	22.1	1.50
	$\mu = 0.3$	14.2	13.4	13.9	22.9	3.73
Continuum model		14.1	13.2	13.1	16.5	0.76

Component radius: 1.31 mm which yields a value of 6.42 10^4 N/mm^2 for Young's modulus of component.

Table 5 presents the results obtained for the different models. Besides the calculated stiffness matrix components, the percentage of asymmetry between coupling terms, $k_{\varepsilon\theta}$ and $k_{\theta\varepsilon}$, is shown for each model. The influence of friction is presented for the Raoof and Leech models. It should be noted that in synthetic fiber ropes, the friction coefficient between the different components is not a well known parameter. For the yarn on yarn, and the aramid material, friction coefficient values are given between 0.11 and 0.24 (FRM, 2003). These values have been obtained from tests on the different yarns.

It should be also mentioned that, in Raoof's model, the packing factor in each layer is assumed to be $\frac{\pi}{4}$ (for metallic components), but here this value is modified by using the value corresponding to that chosen in the

Fig. 8. Testing of yarns on 10 kN test machine, two digital cameras to measure strain.

FRM software, as well as the global packing factor for the continuum model. Indeed, the same structure is defined for all the models (same material quantity in the structure).

The main conclusion from Table 5 is that all the models yield very similar results for the axial stiffness, $k_{\varepsilon\varepsilon}$. The difference for the coupling terms is visible. Only the torsion term results, $k_{\theta\theta}$, are significantly different for the different models.

To show which model gives more reliable results (particularly for the torsion term, $k_{\theta\theta}$), it would be necessary to be able to compare them to experimental results.

In Raoof's model, the structure in the no-slip case is much stiffer than in full-slip, however the coupling terms are smaller in the no-slip case. On the other hand, except for the axial stiffness where the two limit case results are similar, the differences between the two cases are significant, particularly for the torsion term. It is interesting to note that the orthotropic sheet theory presented for the multilayered metallic cables by Raoof, and based on the contact theory between the metallic components with circular cross-section, yields results completely comparable with those obtained from other specific models for synthetic cables.

The model of Hoppe provides a similar value for the axial stiffness but does not allow the other stiffness terms to be obtained.

The results from Leech's model show that the friction effect can be neglected for axial loading. However, it should be mentioned that while the friction effect plays a small role in global stiffness behavior of such structures, the effect of friction on the long-term performance and durability of a structure under cyclic loading can be significant.

Then, the theoretical predictions will be compared to experimental results which are obtained from traction test on two different structures.

6. Experimental results

Experimental studies have been performed at two scale levels, first on yarns to determine the base component properties and then on two different assembled yarns which represent the multilayer structure.

Tensile tests at the yarn level give an indication of the material behavior without the effects of twist and construction. They were performed on a 10 kN test machine at an applied crosshead displacement rate of 50 mm/min. Elongation was measured using two digital cameras, which record the movements of marks on the yarns, as shown in Fig. 8. The test procedure for these and all subsequent tests was to apply five bedding-in load–unload cycles up to 50% of the nominal break load, before the load cycle which was used for the modeling. This is standard practice in rope testing and stabilizes the material and construction.

An example of the yarn test results including the five bedding-in cycles and the test to failure is shown in Fig. 9.

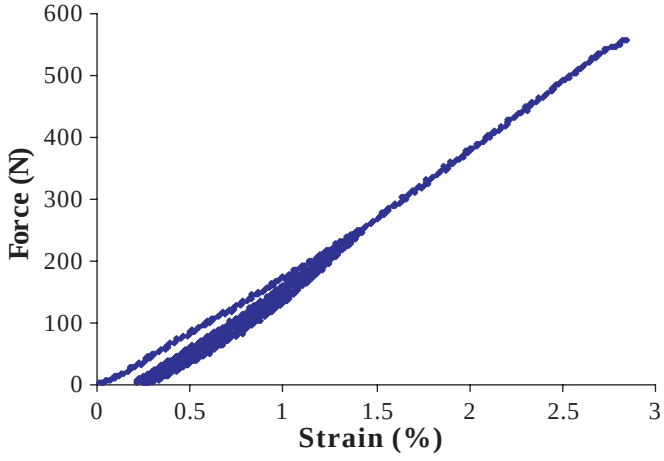

Fig. 9. Force–strain plot for tensile test on 336 tex aramid yarn (Twaron 1000), five cycles to 50% of break load followed by test to failure.

Chailleux and Davies (2003) have also used yarn tests to identify the intrinsic viscoelastic and viscoplastic behaviour of the aramid fibers used in the present study (Twaron 1000).

In order to provide data for correlation with the models, tests were then performed on two different assembled yarns taken from a 25 ton break load rope, Fig. 10 (at least five specimens were characterized for each), for which the construction parameters are given in Table 6. All the samples were made with the same aramid fiber grade. The load was introduced through cone and spike end connections. Tests involved applying five initial bedding-in cycles, as for the yarn tests, by loading the samples to 50% of their nominal break load at a loading and rate of 50 mm/min then unloading at the same rate. The same image analysis system was used, measuring the displacements of two marks bonded to the assembled yarn (Fig. 10). From the tests

Fig. 10. Test on assembled yarn sample on 200 kN test machine, showing sample and two digital cameras to measure strain.

Table 6
Construction parameters for different structures

Structure	Construction parameters		Structure	Construction parameters	
Assembled yarn 1	Outer diameter	2.03 (mm)	Assembled yarn 2	Outer diameter	2.33 (mm)
	Component diameter	0.572 (mm)		Component diameter	0.572 (mm)
	Pitch length	52.6 (mm)		Pitch length	58.8 (mm)
	Component number	12		Component number	16
	Component axial stiffness, k_c	21.4 kN		component axial stiffness, k_c	21.4 kN

Table 7
Test results on the yarns and assembled yarns after five bedding-in cycles

Samples	Test number	Sample length (mm)	Average axial stiffness (kN)	Average rupture force (kN)
Yarn (Twaron 1000)	5	349–355	$21.4 \pm 1\%$	$0.550 \pm 2\%$
Assembled yarn 1	6	344–352	$228.2 \pm 3.6\%$	$5.12 \pm 8\%$
Assembled yarn 2	5	343–354	$298.5 \pm 0.8\%$	$6.88 \pm 14\%$

on the component (yarn) and the structures (assembled yarns 1 and 2) the axial stiffness values were measured as shown in Table 7. The stiffness values presented are those from the 6th loading.

7. Comparison between prediction and tests

In this section the previous experimental results will be compared to models predictions. For modeling the assembled yarn 1, the number of layers is assumed to be 2, for which the component numbers for each layer are 3 and 9. The PF's for each layer are both 0.95, and the corresponding global packing factor, from Eq. (28), is also 0.95. In the assembled yarn 2, the number of layers is assumed to be 3 in which the component numbers for each layer are 1, 5 and 10. The PF's in each layer are 1, 0.96 and 0.96 respectively and the corresponding global packing factor, from Eq. (28), is 0.96.

The yarn axial stiffness and the geometrical parameters then enable a prediction to be made of the stiffness coefficients of the structures using the continuum model (Eq. $(29)_1$), and this gives axial stiffness values of 252.7 kN and 336.7 kN for assembled yarns 1 and 2 respectively. The structures were also modeled with the FRM software, and this gives results very close to those of the continuum model (252.6 kN and 336.9 kN respectively). Raoof's model was not applied to these structures because there are not a large number of wires in each of the layers here.

The comparison is shown graphically in Fig. 11.

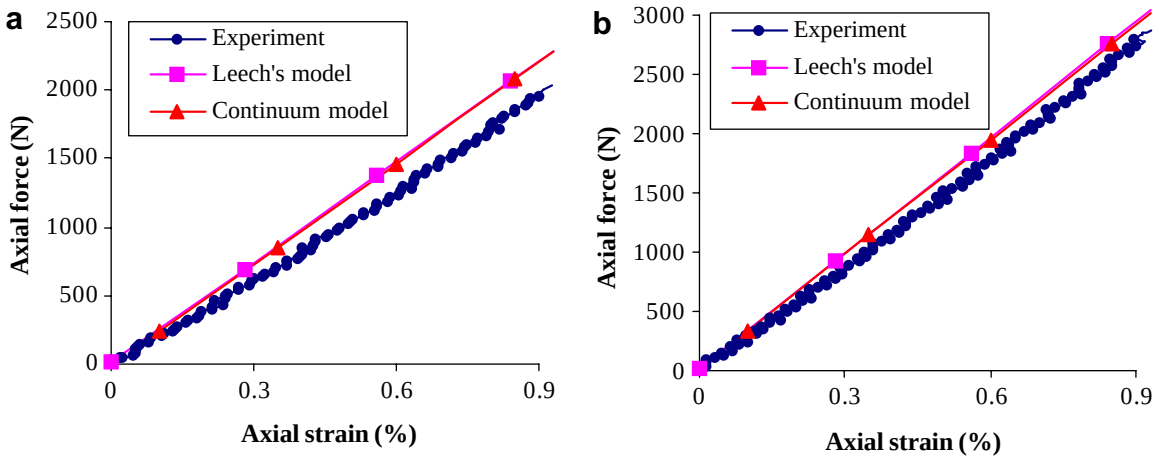

Fig. 11. Comparison between present model predictions, FRM software results and corresponding experimental measurements for force–strain curve of (a) assembled yarn 1 and (b) assembled yarn 2.

So far all the tests performed have concentrated on the axial stiffness $k_{\varepsilon\varepsilon}$ by testing structures with fixed end loading conditions. However, a small number of tests have shown that there is not measurable tension–torsion coupling terms and torsion stiffness for the small diameter assembled yarns at this level. In order to determine the other coefficients (coupling terms and torsion term) and to compare them with predicted values test results for the higher level such as strands of 205 T fiber rope would be necessary.

8. Conclusion

A non-linear elastic continuum model has been developed for the analysis of the overall axial stiffness of fibrous structures with a large number of twisted components. By contrast with multilayered approaches, the structure under consideration is herein depicted as a set of coaxial helixes only characterized by their external lay angle and corresponding radius. The constitutive material is assumed to be linear. Static monotonic axial loads are considered, the inter-fiber friction effects are not taken into account. Moreover, the studied structures exhibiting small lay angles, the overall diametral contractions are neglected, which may contribute to the overestimation of stiffness. The analytical model developed leads to useful closed-form expressions thus allowing rope constructions to be optimized.

Due to lack of published experimental data, the model has first been compared with models of the literature. The results obtained, have shown that all the models give results that agree reasonably well with each other, except with respect to the torsion stiffness, for which there is a significant difference. In addition, stiffness matrices of all the models deviate slightly from symmetry and this lack of symmetry is due to a certain lack of consistency in the various simplifying hypotheses.

Tensile tests have then been performed on aramid fiber assemblies with two structures, to obtain the axial stiffness. The preliminary test results indicate a good correlation with the model. Additional test data, especially to examine tension–torsion and pure torsion loading, are needed to gauge performance of the models. The integration of these results in a model for a large aramid wire rope and comparison with tension and tension–torsion coupling test results will be described in Part II (Ghoreishi et al., in press) of this paper.

References

Beltran, J.F., Rungamornrat, J., Williamson, E.B., 2003. Computational model for the analysis of damage ropes. In: Proceedings of The thirteenth International Offshore and Polar Engineering Conference, Honolulu, Hawai, USA.

Beltran, J.F., Williamson, E.B., 2004. Investigation of the damage-dependent response of mooring ropes. In: Proceedings of The Fourteenth International Offshore and Polar Engineering Conference Toulon, France.

Blouin, F., Cardou, A., 1989. A study of helically reinforced cylinders under axially symmetric loads mathematical modelling. International Journal of Solids and Structures. 25 (2), 189–200.

Chailleux, E., Davies, P., 2003. Modelling the non-linear viscoelastic and viscoplastic behaviour of aramid fiber yarns. Mechanics of Time Dependent Materials Journal 7 (3–4), 291–303.

Crossley, J.A., Spencer, A.J.M., England, A.H., 2003a. Analytical solutions for bending and flexure of helically reinforced cylinders. International Journal of Solids and Structures 40 (4), 777–806.

Crossley, J.A., England, A.H., Spencer, A.J.M., 2003b. Bending and flexure of cylindrically monoclinic elastic cylinders. International Journal of Solids and Structures 40 (25), 6999–7013.

Foster, G.P., 2002. Advantages of fiber rope over wire rope. Journal of Industrial Textiles 32 (1), 67–75.

FRM, Fibre Rope Modeller, version 1.1.5, 2003. Software development for Tension Technology International Ltd. (TTI).

Ghoreishi, S.R., 2005. Modélisation analytique et caractérisation expérimentale du comportement de câbles synthétiques. Ph.D. Thesis, Ecole Centrale de Nantes, France.

Ghoreishi, S.R., Davies, P., Cartraud, P., Messager, T., in press. Analytical modeling of synthetic fiber ropes, part II: A linear elastic model for $1 + 6$ fibrous structures. International Journal of Solids and Structures, doi:10.1016/j.ijsolstr.2006.08.032.

Hobbs, R.E., Raoof, M., 1982. Interwire slippage and fatigue prediction in stranded cables for TLP tethersBehaviour of Offshore Structures, 2. Hemisphere publishing/McGraw-Hill, New York, pp. 77–99.

Hoppe, L.F.E., 1991. Modeling the Static Behavior of Dyneema in Wire-rope Construction. MTS RTM.

Jolicoeur, C., Cardou, A., 1994. An analytical solution for bending of coaxial orthotropic cylinders. Journal of Engineering Mechanics 120 (12), 2556–2574.

Jolicoeur, C., Cardou, A., 1996. Semicontinuous mathematical model for bending of multilayered wire strands. Journal of engineering Mechanics 122 (7), 643–650.

Leech, C.M., 2002. The modeling of friction in polymer fibre rope. International Journal of Mechanical Sciences. 44, 621–643.

Leech, C.M., Hearle, J.W.S., Overington, M.S., Banfield, S.J., 1993. Modelling tension and torque properties of fibre ropes and splices. In: Proceeding of the Third International Offshore and Polar Engineering Conference Singapore.
Mindlin, R.D., 1949. Compliance of elastic bodies in contact. Journal of Applied Mechanics 16, 259–268.
Raoof, M., 1983. Interwire contact forces and the static, hysteretic and fatigue properties of multi-layer structural strands. Ph.D. Thesis, Imperial College of Science and Technology, London, UK.
Raoof, M., 1991. Method for analysing large spiral strands. Journal of Strain Analysis 26 (3), 165–174.
Raoof, M., Hobbs, R.E., 1988. Analysis of multilayered structural strands. Journal of engineering Mechanics 114 (7), 1166–1182.
Raoof, M., Kraincanic, I., 1995a. Simple derivation of the stiffness matrix for axial/torsional coupling of spiral strands. Computers and Structures 55 (4), 589–600.
Raoof, M., Kraincanic, I., 1995b. Analysis of large diameter steel ropes. Journal of Engineering Mechanics 121 (6), 667–675.
Rungamornrat, J., Beltran, J.F., Williamson, E.B., 2002. Computational model for synthetic-fiber rope response. In: Proceeding of Fifteenth Engineering Mechanics Conference. ASCE, New York.